Journal of Applied Fluid Mechanics, Vol. 17, No. 8, pp. 1687-1704, 2024.
Available online at www.jafmonline.net, ISSN 1735-3572, EISSN 1735-3645.
https://doi.org/10.47176/jafm.17.8.2492

CPFD Simulation of Hydrodynamic Characteristics of Multiple Particles Mixing in a Circulating Fluidized Bed

Q. X. Xiong and L. Zheng†

School of Energy and Power Engineering, Nanjing University of Science and Technology, Nanjing 210094, China

†Corresponding Author Email: lz@njust.edu.cn

ABSTRACT

Computational particle fluid dynamics method is utilized to study the influence of polydisperse and monodisperse particle size distribution, fuel addition, and biomass mixing ratio on the gas-solid flow behavior in a pilot-scale circulating fluidized bed (CFB). Numerical results show that a polydisperse system with different particle sizes can enhance the fluidization quality and the uniformity of the particle volume fraction in comparison with a monodisperse system with uniform particle sizes. When fuel is present in the CFB, the disturbance at the circulation inlet is eliminated and the particle aggregation effect at the wall is reduced. Furthermore, the particle volume fraction, pressure, and particle velocity distributions change only slightly as the biomass increased from 0% to 20% or from 50% to 100% of the total fuel mass. However, as the biomass ratio increases from 20% to 50%, the pressure drop in the riser decreases and the back-mixing degree at the riser wall weakens.

Article History

Received December 7, 2023
Revised February 21, 2024
Accepted March 12, 2024
Available online May 29, 2024

Keywords:

CPFD
Hydrodynamics
Circulating fluidized bed
Particle size distribution
Multiple particles mixing

1. INTRODUCTION

Circulating fluidized beds (CFBs) have received widespread attention as an important energy-conversion technique in many industrial processes, including coal combustion, biomass gasification, and fluid catalytic cracking (Zhu et al., 2019). Owing to the full mixing of the gas and solid phases, CFBs have distinct advantages such as high combustion efficiency, wide fuel adaptability, and excellent heat- and mass-transfer performance (Liu et al., 2022). Therefore, numerous experiments and simulations have been conducted to comprehensively understand the flow characteristics between gas and solid phases in CFBs.

Zhu et al. (2020) investigated the hydrodynamic behavior of a pilot-scale pressured CFB using electrical capacitance tomography. Carlos et al. (2017) used particle image velocimetry and digital image analysis to investigate the flow characteristics of risers. Experimental studies provide valuable insights into the overall flow behavior of CFBs; however, they require sophisticated and costly detection techniques to capture the particle motion. With the advancement of computer technology, computational fluid dynamics (CFD) simulations have become a cost-effective method for studying complex gas-solid flow phenomena in CFB systems (Liu & Wachem, 2019). CFD simulations not only provide detailed information about local flow features, such as particle velocity, concentration, and pressure distribution, but can also be used to explore alternative fuels, evaluate the influence of operating conditions, and develop cleaner and more efficient CFB processes.

In general, the application of CFD simulations to gas-solid flows in CFBs can be divided into two categories: Eulerian-Eulerian and Eulerian-Lagrange schemes (Alobaid, 2015). In the Eulerian-Eulerian scheme, the two-fluid model (TFM) based on the kinetic theory of particle flow is the most representative. Nikolopoulos et al. (2013) compared the full-loop pressure distribution in a CFB using the EMMS and Gidaspow drag models. Liu et al. (2015) examined the effects of varying the solid content and the valve opening or closing dynamics on the axial voidage and solid flux in the riser. Their results qualitatively match the experimental observations. Owing to the assumption that the solid phase is a pseudo-fluid, the TFM method has difficulties simulating flow behaviors using particle size distributions (Mathiesen et al., 2000). Conversely, the Euler-Lagrange scheme, represented by CFD combined with the discrete-element method (CFD-DEM), tracks individual particles and resolves high-frequency collisions. Luo et al. (2015) investigated gas-solid full-loop motions in a three-dimensional CFB and found that the particles rose in an S-shaped path in the riser and spiraled down in the cyclone. Yang et al. (2019a) investigated the dynamic evolution of particle clusters over time and space in a CFB with six parallel cyclones via CFD–DEM. However, CFD–DEM can be computationally intensive, especially when dealing with a large number of particles (Yang & Wang, 2020). To improve the computational efficiency, a hybrid Eulerian-

NOMENCLATURE

C_d	drag coefficient	α_a	gas volume fraction
d_s	particle diameter	α_s	particle volume fraction
e_n	normal-to-wall retention coefficient	α_a	gas volume fraction
e_t	tangent-to-wall retention coefficient	α_{cs}	particle volume fraction at close packing
g	pressure	μ_a	gas viscosity
Re_s	particle Reynolds number	ρ_a	gas velocity
u_a	gas velocity	ρ_s	particle density
u_s	particle velocity	τ_a	gas stress tensor
$u_{s.n}$	normal velocity	τ_s	particle normal stress
$u_{t.n}$	tangential velocity		

Lagrangian scheme, the computational particle fluid dynamics (CPFD) method, has been proposed. The CPFD method introduces the concept of computational particles (Ma et al., 2017; Dong et al., 2021; Bandara et al., 2022) with multiple real particles having the same material properties, physical motions, and chemical changes. Furthermore, the CPFD method employs continuum spatial gradients to handle particle collisions, thereby significantly reducing the simulation time. Numerous studies have demonstrated that the CPFD method can effectively predict the behavior of gas-solid flows in CFBs. Chen et al. (2013) modeled the motion of Geldart A and B particles in a rectangular conduit and observed a nonuniform structure with a dilute upper part and a dense lower part. However, CPFD using a conventional drag model yields less accurate results than the TFM using an energy-minimizing multiscale (EMMS) drag model. Dymala et al. (2021) validated the applicability of the EMMS drag model by performing full-loop CFB simulations. The time-averaged axial solid concentration, circulation rate, and riser pressure drop agreed well with the experimental data. Yang et al. (2019b) analyzed the flow characteristics of Geldart A particles in a CFB equipped with a louvre baffle structure. The louvre baffle effectively suppressed solid back-mixing and divided the bubbles at a low superficial gas velocity.

Table 1 provides a detailed summary of recent numerical studies on the gas-solid flow characteristics in CFBs. A comparative analysis of the literature reveals that the simulation objects are mainly CFBs with different structures or a certain component of the CFB. The effects of operational and simulation parameters such as aeration, pressure, and drag model have been extensively studied. The particle types involved in the simulations are Geldart A, B, and D particles. Cold simulations inside a CFB are normally performed based on the assumption of the particle mean property; however, this inevitably introduces errors. Therefore, a detailed analysis of the differences in flow behavior between particles with uniform sizes and those with a particle size distribution is necessary. In addition, most of the current CFB simulations are for only one type of particle. In industrial processes, the solid phase comprises various particles. For example, in the co-combustion of coal and biomass in CFBs, there are multiple particles with different size distributions, including bed materials (e.g., ash and sand), feed fuel, desulfurizers, desulfurization products, and the ash generated after fuel combustion. It is necessary to further develop numerical simulations of multicomponent particle flows in CFBs to explore the corresponding flow characteristics. Therefore, this study aims to comprehensively analyze the effects of particle size distribution and fuel addition on the gas-solid characteristics in a CFB using the CPFD method. First, we compared the differences in the gas-solid flow characteristics in a CFB between a monodisperse system with a uniform particle size and a polydisperse system with different particle sizes. Additional fuel was then introduced to reveal the effects of different coal and biomass particle proportions on the flow characteristics in the CFB. The remainder of this paper is organized as follows. Section 2 provides an overview of the numerical model used in this study. The physical problem under investigation is described in Section 3. The results and discussion are presented in Section 4. Finally, Section 5 concludes the paper.

2. COMPUTATIONAL MODEL

2.1 Governing Equations

The main objective of this study was to numerically investigate the gas-solid flow characteristics in a CFB. Chemical reactions and heat and mass transfer were not considered. The continuity and momentum equations for the gas phase are respectively formulated as (Almuttahar & Taghipour, 2008a)

$$\frac{\partial}{\partial t}\left(\alpha_g \rho_g\right) + \nabla \cdot \left(\alpha_g \rho_g \boldsymbol{u}_g\right) = 0 \tag{1}$$

$$\frac{\partial}{\partial t}\left(\alpha_g \rho_g \boldsymbol{u}_g\right) + \nabla \cdot \left(\alpha_g \rho_g \boldsymbol{u}_g \boldsymbol{u}_g\right) = -\nabla P + \alpha_g \rho_g \mathbf{g} + \nabla \cdot \left(\alpha_g \tau_g\right) + \boldsymbol{F} \tag{2}$$

where α_g is gas volume fraction, ρ_g is the gas density, $\boldsymbol{u}_g$ is the gas velocity, P is pressure, $\mathbf{g}$ is the gravitational acceleration, τ_g is the gas stress tensor. $\boldsymbol{F}$ is the momentum exchange rate per unit volume between gas and particle phases.

Because the flow is assumed to be isothermal, the density of the gas phase is only a function of pressure and can be calculated using the ideal gas state equation as follows:

$$\rho_g = \frac{P}{RT} \tag{3}$$

τ_g and $\boldsymbol{F}$ are defined by (Fan et al., 2004)

$$\tau_g = \mu_g \left(\frac{\partial \boldsymbol{u_i}}{\partial x_j} + \frac{\partial \boldsymbol{u_j}}{\partial x_i}\right) - \frac{2}{3}\mu_g \frac{\partial \boldsymbol{u_k}}{\partial x_k}\delta_{ij} \tag{4}$$

$$\boldsymbol{F} = \iint f \left\{ m_s \left[D\left(\boldsymbol{u}_g - \boldsymbol{u}_s\right) - \frac{\nabla P}{\rho_s} \right] \right\} dm_s d\boldsymbol{u}_s \tag{5}$$

Table 1 Summary of numerical simulations of gas-solid flow characteristics in CFBs

Authors and Year	Simulation methods	Types of particles	Aim
Nikolopoulos et al. (2013)	TFM	Geldart B	The EMMS and the Gidaspow drag models
Chen et al. (2013)	CPFD	Geldart A, Geldart B	Two-dimensional and three-dimensional CFB riser, TFM and CPFD, different drag models
Li et al. (2014)	TFM	Geldart B	Full-loop and riser-only
Wang et al. (2014a)	CPFD	Geldart B	Mesh size, close pack volume fraction, interphase drag model and particle size distribution
Wang et al. (2014b)	CPFD	Geldart B	Loop seal aeration rate, fluidized air velocity and total bed inventory
Liu et al. (2015)	TFM	Geldart A	The dynamic change of the opening or closing of the valve, different solids inventories, the variation of axial voidage profile and solids flux
Luo et al. (2015)	DEM	Geldart D	The particle-scale details related to solid motion, the superficial velocity
Tu and Wang (2017)	CPFD	Geldart B	Wen-Yu and EMMS drag models for a complex CFB with six cyclones
Ma et al. (2017)	CPFD	Geldart B	Pressure distribution and solids circulation rate under different aeration conditions of the standpipe.
Yang et al. (2018)	CPFD	Geldart A	With and without baffles
Wang et al. (2018)	DEM	Geldart A	Superficial gas velocities in a square cross-section CFB
Yang et al. (2019a)	DEM	Geldart D	Focus on the cluster behavior, flux and granular temperature.
Zhu et al. (2019)	CPFD	Geldart B	Volume fraction distribution, velocity and circulation flux in a pressured CFB
Yang et al. (2019b)	CPFD	Geldart A	A method to characterize solids back-mixing strength, the effects of louver baffles
Zhang et al. (2020)	CPFD	Geldart B	Exit geometry of riser
Yang and Wang (2020)	CPFD	Geldart B	Superficial gas velocities
Dong et al. (2021)	CPFD	Geldart B	Different operating pressures
Dymala et al. (2021)	CPFD	Geldart B	Rectangular and cylindrical risers, EMMS and Wen-Yu/Ergun drag models
Córcoles et al. (2021)	CPFD/TFM	Geldart B	Frequency analysis, bubble pierced length, bubble size, bubble passage frequency and bubble velocity, Comparison of TFM and CPFD
Sung et al. (2021)	CPFD	Geldart B	Correction factor of drag coefficient, the standard deviation of log normal distribution
Bandara et al. (2022)	CPFD	Geldart B	Loop seal aeration, riser aeration, sand particle sizes

where μ_g is the shear viscosity, δ_{ij} is the Kronecker function, $\boldsymbol{u}_s$ is the particle velocity, m_s is the particle mass and ρ_s is the particle density. D is a drag function. The probability distribution function f, which is used to characterize the hydrodynamics of the solid phase, can be derived through the Liouville equation as follow (Fan et al., 2004):

$$\frac{\partial f}{\partial t} + \nabla \cdot (f\boldsymbol{u}_s) + \nabla_{\boldsymbol{u}_s} \cdot (f\boldsymbol{A}) = 0 \tag{6}$$

where $\boldsymbol{A}$ is particle acceleration, which in turn is defined as

$$\boldsymbol{A} = \frac{d\boldsymbol{u}_s}{dt} = D\left(\boldsymbol{u}_g - \boldsymbol{u}_s\right) - \frac{1}{\rho_s}\nabla P - \frac{1}{\alpha_s \rho_s}\nabla \tau_s + \mathbf{g} \tag{7}$$

where α_s is the particle volume fraction, and τ_s is the particle normal stress. The value of α_s and τ_s can be respectively obtained by (Snider, 2001)

$$\alpha_s = \iint f \frac{m_s}{\rho_s} dm_s d\boldsymbol{u}_s \tag{8}$$

$$\tau_s = \frac{P_s \alpha_s{}^{\beta}}{max[(\alpha_{cs} - \alpha_s),\ \delta(1-\alpha_s)]} \tag{9}$$

where P_s is a positive constant with units of pressure, β is a constant chosen between 2 and 5, α_{cs} is particle volume fraction at close packing, and δ is a small number on the order of 10^{-7} to avoid the singularity at the close packing state.

2.2 Drag Model

The momentum interaction between the gas and solid phases is mainly reflected in the drag force, and the choice of the drag model is very important for accurately representing the gas-solid flow characteristics in a CFB.

Different flow regimes exist, and the solid volume fraction changes from a dilute to a close-packed state for full-loop simulations. In the literature, the Wen-Yu drag model is frequently used for solid volume fractions below $0.75\alpha_{cs}$, while the Ergun model is used when the solid volume fraction is larger than $0.85\alpha_{cs}$. In this study, a combination of the Wen-Yu and Ergun models was adopted, and the expression is given as (Yang et al., 2019b)

$$D = \begin{cases} D_1 = \frac{3}{4} C_d \frac{\rho_g}{\rho_s} \frac{|\boldsymbol{u_g} - \boldsymbol{u_s}|}{d_s} & \alpha_s < 0.75\alpha_{cs} \\ (D_2 - D_1)\left(\frac{\alpha_s - 0.75\alpha_{cs}}{0.85\alpha_{cs} - 0.75\alpha_{cs}}\right) + D_1, & 0.75\ \alpha_{cs} \le \alpha_s \le 0.85\alpha_{cs} \\ D_2 = \left(\frac{180\alpha_s}{\alpha_g Re_s} + 2\right) C_d \frac{\rho_g}{\rho_s} \frac{|\boldsymbol{u_g} - \boldsymbol{u_s}|}{d_s} & \alpha_s > 0.85\alpha_{cs} \end{cases} \tag{10}$$

where d_s is the particle diameter and C_d is the drag coefficient, which is defined as

$$C_d = f(x) = \begin{cases} \frac{24}{Re_s}(1 + 0.15Re_s^{0.687}) & Re_s < 1000 \\ 0.44 & Re_s \ge 1000 \end{cases} \tag{11}$$

where Re_s is the particle Reynolds number, whose definition is

$$Re_s = \frac{\alpha_s \rho_g |\boldsymbol{u_g} - \boldsymbol{u_s}| d_s}{\mu_s} \tag{12}$$

2.3 Boundary Conditions

The model employed a velocity inlet boundary condition for the gas-phase field and a mass-flow boundary condition for the solid phase field. Pressure outlet boundary condition was set at the cyclone outlet. A non-slip boundary condition was applied to gas phase. Incomplete elastic collisions are used for the interaction between discrete particles and wall (Harris & Crighton, 1994)

$$\boldsymbol{u}_{s,n}^{i+1} = -e_n \boldsymbol{u}_{s,n}^{i} \tag{13}$$

$$\boldsymbol{u}_{s,t}^{i+1} = e_t \boldsymbol{u}_{s,n}^{i} \tag{14}$$

where $\boldsymbol{u}_{s,n}$ and $\boldsymbol{u}_{t,n}$ are the normal and tangential velocities, respectively, and e_n and e_t are the normal-to-wall retention coefficient and tangent-to-wall retention coefficient, respectively.

3. PHYSICAL PROBLEM

In this study, the full-loop gas-solid flow characteristics in a pilot-scale cold CFB system consisting of various components, such as risers, cyclones, standpipes, and loop seals (Yang & Wang, 2020), were investigated. Figure 1 depicts simplified three-dimensional schematic of the CFB. The height of the riser was 6500 mm, and the diameters of the riser, cyclone, and standpipe were 200, 350, and 120 mm, respectively. In terms of the boundary conditions, primary air (U1) was introduced through the distributor located at the bottom of

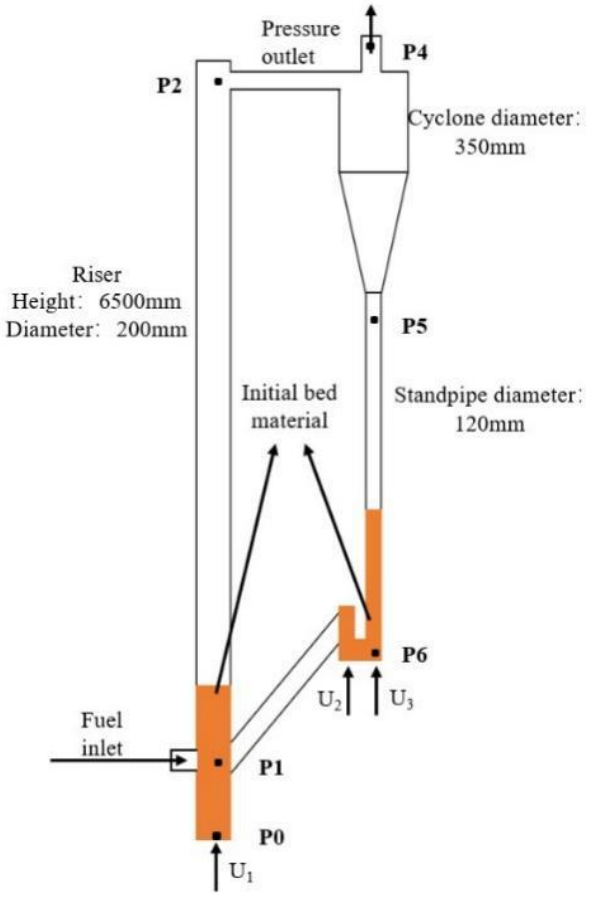

Fig. 1 Schematic diagram of the circulating fluidized bed

Table 2 Simulation parameters and operation conditions

Parameters	Value
Gas density	1.18 kg/m^3
Gas viscosity	1.84×10^{-5} Pa·s
Turbulence model	LES
Closed pack volume fraction	0.6
Normal-to-wall retention coefficient	0.3
Tangent-to-wall retention coefficient	0.99
Maximum momentum redirection from collision	40%
Fluidized gas velocity	U_1: 7 m/s, U_2: 0.3 m/s, U_3: 0.15 m/s
Diffuse bounce	0
Initial time step	0.0005 s
Total time	35 s
Averaging start time	20 s

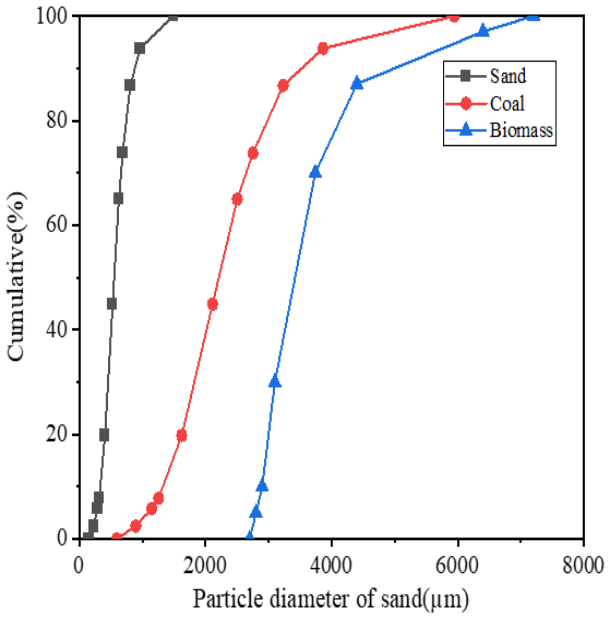

Fig. 2 Particle size distributions of sand, coal, and biomass

the riser, while loose air (U2) and return air (U3) were introduced separately from the bottom of the supply and recycle chambers of the loop seal. The top plane of the cyclone served as the pressure outlet boundary. Multiple transient pressure points were designated and marked for analysis. Initially, the bed material (sand) is packed into the riser and loop seal.

During the simulations, fuel was continuously supplied 37 mm above the distribution plate, and the fuel particles consisted of coal and biomass. The densities of the materials were set as follows: sand, 2600 kg/m^3; coal, 1346 kg/m^3; and biomass, 700 kg/m^3. The particle size distribution of each particle type is shown in Fig. 2. The other parameters and operational conditions are listed in Table 2.

4. RESULTS AND DISCUSSION

4.1 Model Validation

The CPFD method was first validated in a 30kW$_{th}$ CFB riser (Gündüz et al., 2020). The height and diameter of the riser are 6 m and 0.108 m respectively. The solid phase was quartz sand and the gas phase was air. The particle density is 2650 kg/m^3, and the density and viscosity of air are 1.2 kg/m^3 and 1.9×10^{-5} Pa·s, respectively. The operating conditions are a constant temperature of 298 K, atmospheric pressure, and superficial gas velocity of 3 m/s. The simulation duration lasted 100 s and the data were averaged after 20 s. Comparing the experimental data and numerical results from previous work (Gündüz et al., 2020), the results shown in Fig. 3 (a) indicate the pressure distribution in the riser is in good agreement with the results of Gündüz et al. Although slightly higher than the experimental results, the relative errors remained below 5%, and the decreasing trend in pressure was better predicted. The radial distributions of the particle volume fractions at various heights in the riser are shown in Fig 3 (b). The numerical results successfully predict a "core-annular" structure in the riser, aligning well with those reported by Gündüz et al. (2020).

In addition, based on the experimental data for the axial velocity and particle volume fraction distribution of the experimental CFB riser at the Chemical Reaction Engineering Laboratory at the University of Washington (Bhusarapu et al., 2006; Shi et al., 2014), An additional simulation was performed to refine the validation section. Figures 3 (c) and (d) show a comparison between the experimental and simulated results for the radial distributions of the particle axial velocity and particle volume fraction for h/H = 0.69. The simulation exhibited a low particle axial velocity. However, the trends in the radial distributions of the particle axial velocity and particle volume fraction were predicted reasonably well. Therefore, the CPFD method can be used to predict the flow characteristics of the riser.

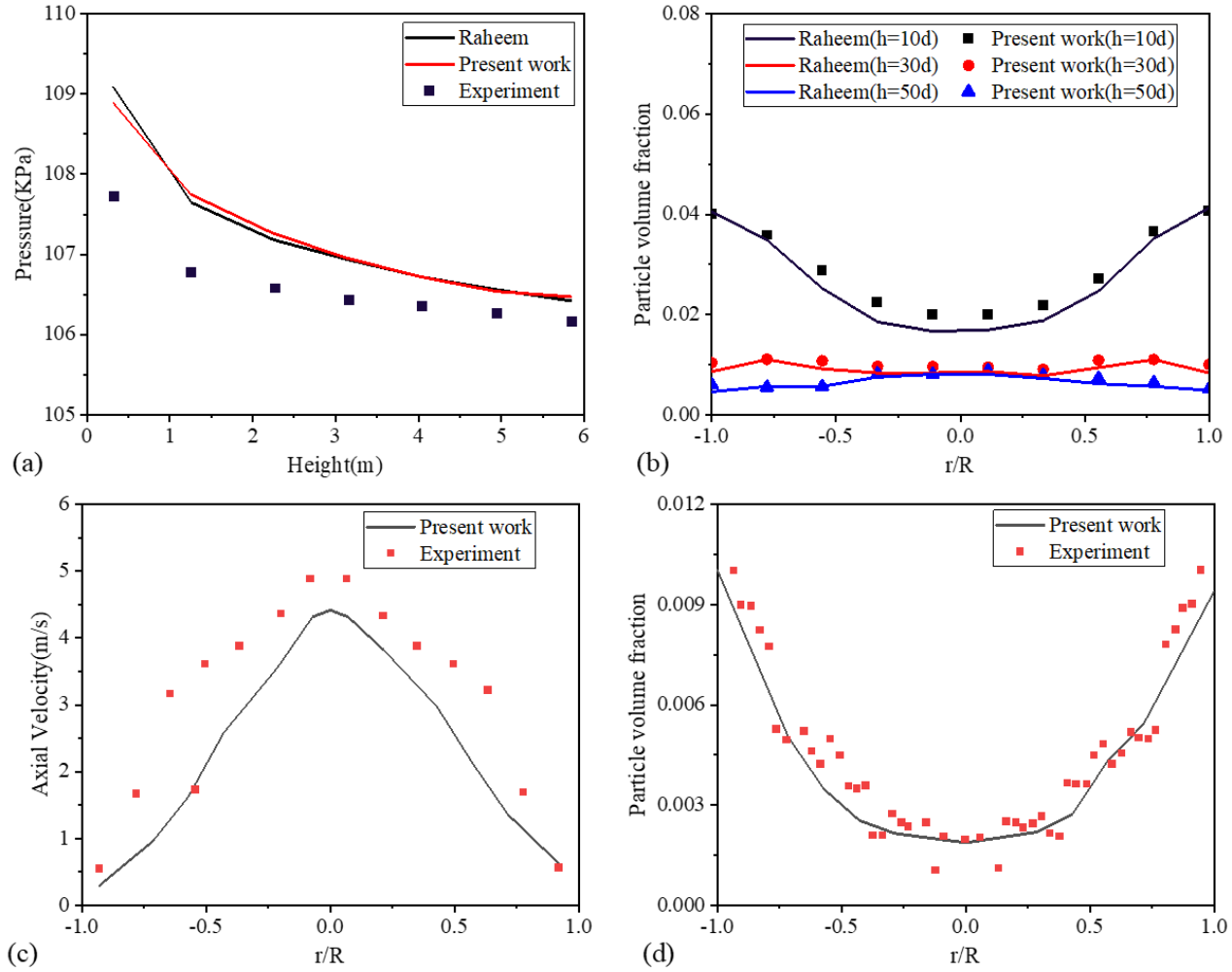

Fig. 3 Model validation results: (a) axial distribution of pressure; (b) radial distribution of particle volume fraction at different heights of the riser by (Gündüz et al., 2020); (c) radial distribution of particle axial velocity; (b) radial distribution of particle volume fraction at h/H=0.69 by (Bhusarapu et al., 2006)

4.2 Grid Independence Analysis

In this study, grid-independence tests were conducted at four different grid resolutions. The total number of grids was 98748, 161280, 287532, and 471408, corresponding to Grid1, Grid2, Grid3 and Grid4, respectively. Figures 4 illustrates the time-averaged pressure as a function of the riser height and the instantaneous particle volume fraction distribution at 35 s for the four grids. Grid1 predicts a significantly higher time-averaged pressure than the other grids and shows particle non-circulation at the loop seal. Therefore, Grid1 is omitted for further analysis. By gradually increasing the grid density from Grid2 to Grid4, especially in key areas such as cyclones and loop seals, the pressure distributions were similar, and the particles in the loop seal entering the riser became smoother. However, an excessive increase in the number of grids leads to a significant increase in computational time and cost. To reach a balance between computational accuracy and cost-effectiveness, Grid3 was chosen for subsequent simulations without loss of accuracy.

In addition, statistical time are closely related to the accuracy of the simulation results. A flux plane was set in the standpipe to monitor the particle circulation rate. Figure 5 shows particle mass flux variation as a function of time. Negative values indicate that the particles are moving in a downward direction. It is noted that the system reaches a steady state after 20 s. For the analysis of the results of all variables, a period of time after the 20 s should be selected for the averaging calculation. The last 20 s (20 s ~ 40 s), 15 s (20 s ~ 35 s), and 10 s (20 s ~ 30 s) of the axial distribution of pressure and particle volume fraction are showed in Fig. 6. The statistical time has a slight influence on the axial distribution of pressure and volume fraction. To obtain a more accurate result, the statistical time is the last 15 s. Therefore, the total simulation time is 35 s.

4.3 Effect of Particle Size Distribution

One significant advantage of the CPFD method for studying solid flow characteristics is the straightforward implementation of a polydisperse particle size distribution. Often in many studies, all particles are assumed to be uniform; however, this does not accurately reflect reality. In this work, we first investigated the effect of different particle size distributions. The particles selected were sand. Two cases were considered: a polydisperse particle size distribution (polydisperse), and a uniform particle size (monodisperse). The Sauter mean diameter of the particles (d_{sauter} = 500 μm) was used, and the polydisperse particle

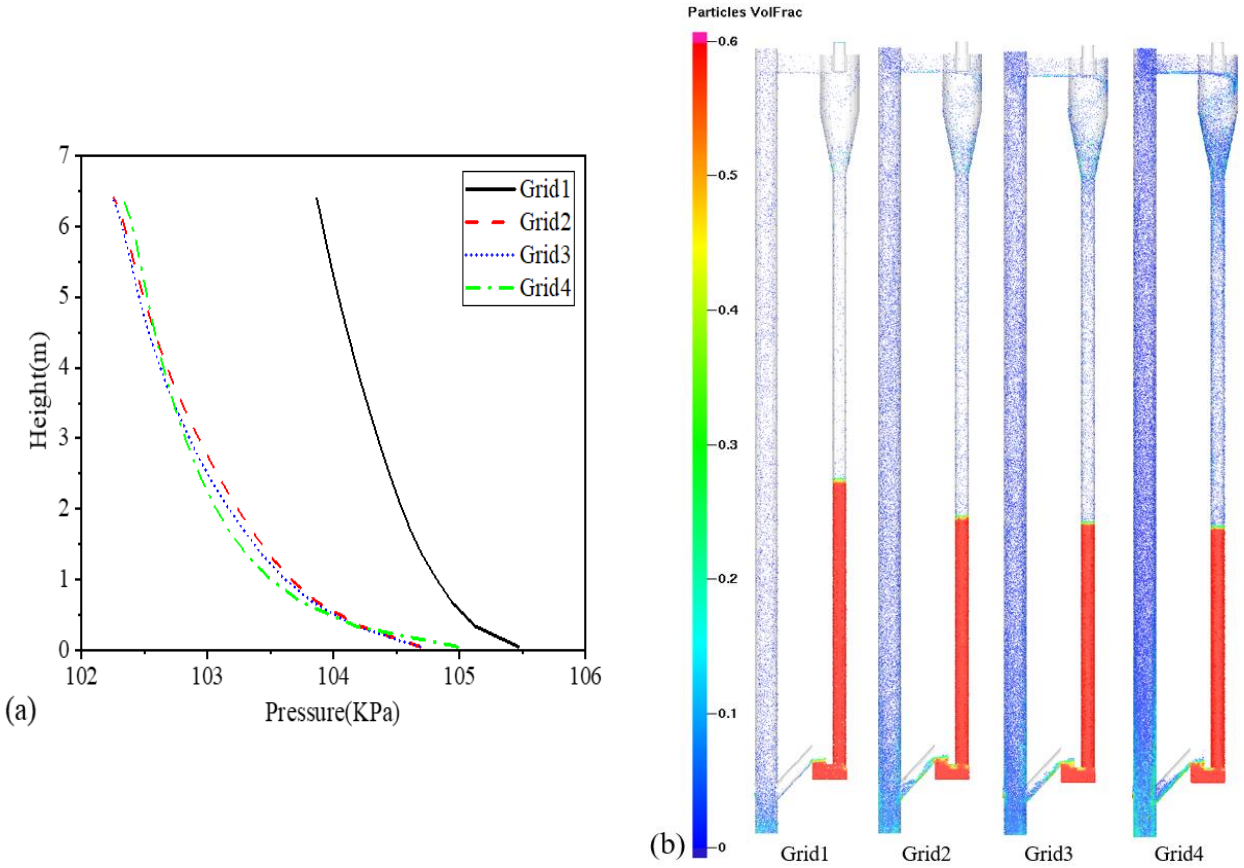

Fig. 4 Grid-independence tests: (a) pressure as a function of height; (b)Instantaneous distribution of particle volume fraction at 35 s for four grids

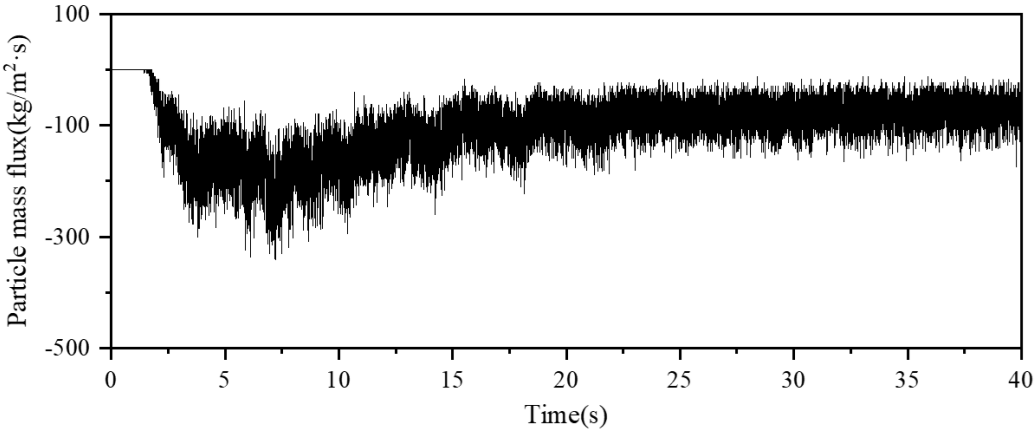

Fig. 5 particle mass flux variation as a function of time in the standpipe

size distribution of the sand is shown in Fig. 2. In CFB systems, the crucial factors that influence the flow characteristics between the gas and solid phases are the particle volume fraction, pressure, and particle velocity (Leboreiro et al., 2008; Almuttahar & Taghipour, 2008b; Lan et al., 2013). Next, we present a detailed discussion of these parameters to better understand their distributions in the CFB system.

4.3.1 Particle Volume Fraction Distribution

Figure 7 shows the variation of particle volume fraction over time in the CFB system. Initially, the particles build up at the bottom of the riser and loop seal. Subsequently, the primary air introduced from the bottom of the riser caused the particles to expand rapidly owing to the intense momentum exchange between the gas and solid phases. The entrapped particles enter the cyclone tangentially and are separated from the gas phase by a large inertial centrifugal force. Eventually, the particles fall into the loop seal and return to the riser via the return air at the bottom of the loop seal. Particles began to accumulate in the standpipe after approximately 3 s, and the particle accumulation height did not change after 20 s, indicating that the CFB system had reached a steady state.

For the subsequent time-averaged results, data

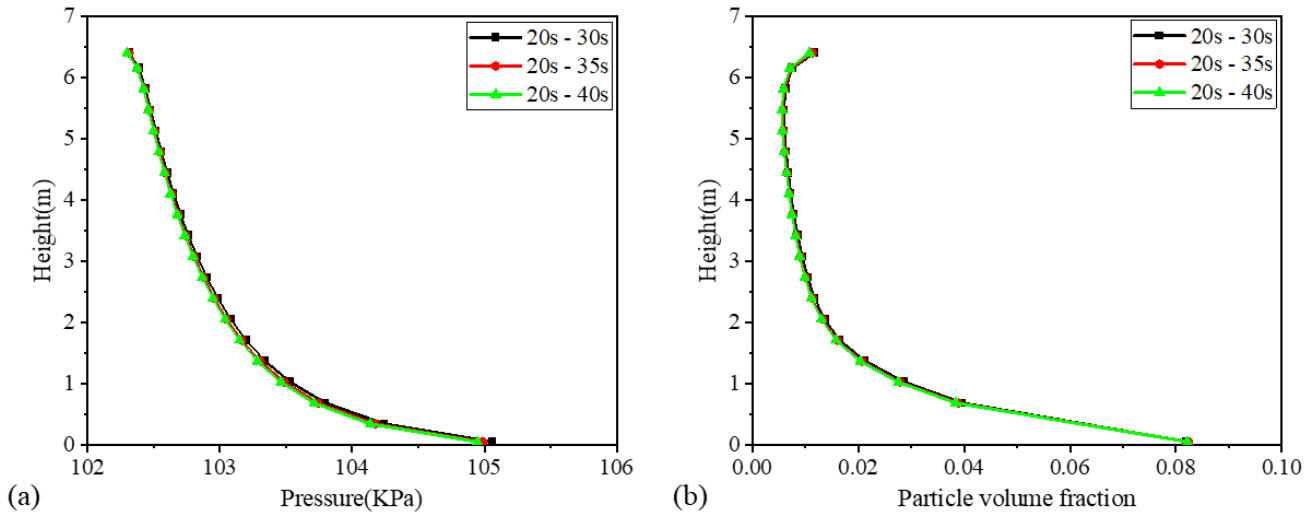

Fig. 6 Axial distribution along the height of riser for different statistical time: (a) pressure; (b) particle volume fraction

Table 3 Comparison of simulation results under different particle size type

Simulation case	Polydisperse	Monodisperse
G_s (kg/m^2·s)	60.50	107.60
Pressure drop in riser (KPa)	2.49	5.89
Particle packed height in the standpipe (m)	2.06	1.35
Pressure drop in the standpipe (KPa)	4.58	7.69
Average pressure gradient in the standpipe (KPa/m)	2.22	5.70

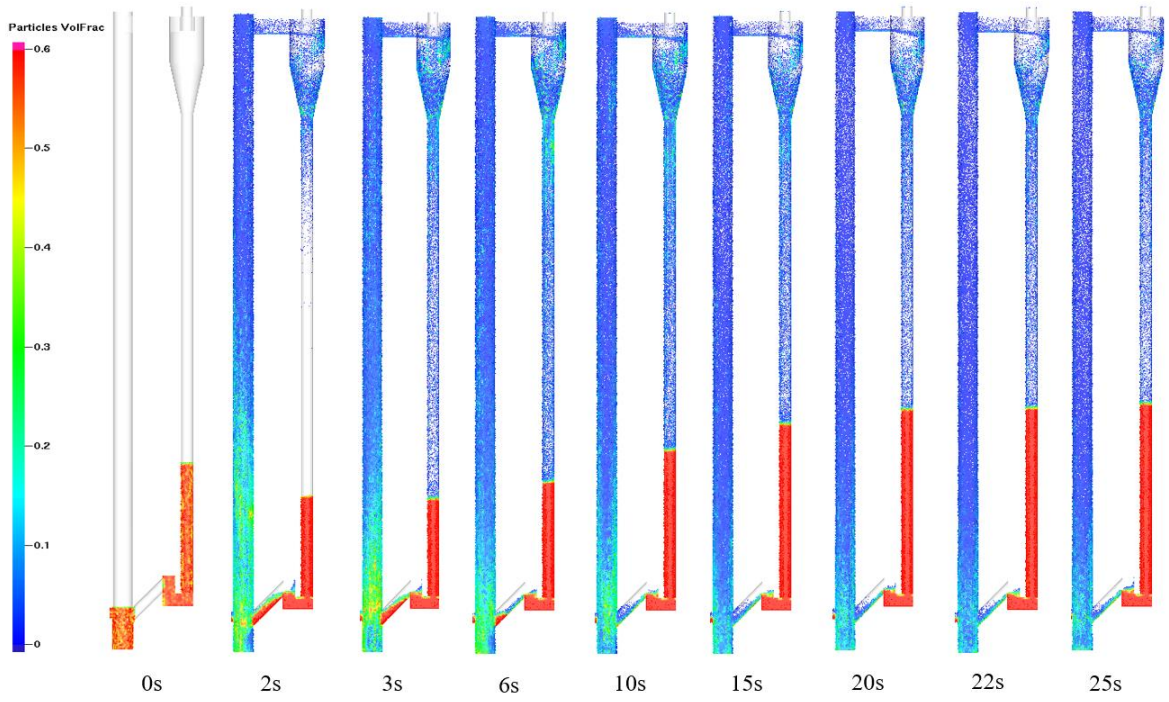

Fig. 7 Evolution of particle volume fraction (polydisperse)

collected after 20 s were averaged. Figure 8 shows the instantaneous distributions of the particle volume fraction and particle radius at 35 s for both the polydisperse and monodisperse cases. Table 3 presents the relevant quantitative results. A significant difference exists in the steady-state particle accumulation height in the standpipe between the two cases. In the monodisperse case, particles tend to agglomerate at the recirculation inlet (Fig. 8(a))

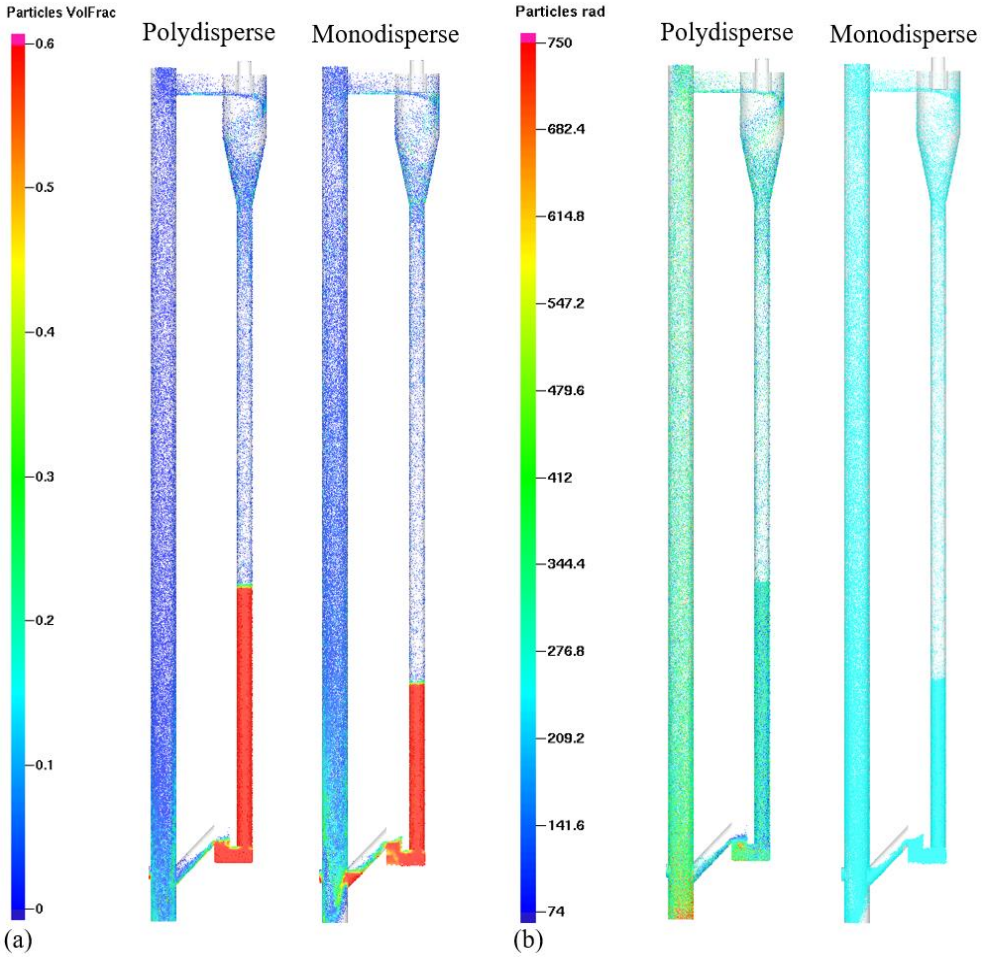

Fig. 8 Instantaneous particle volume fraction and particle radius distributions at 35th second: (a) particle volume fraction distribution; (b) particle radius distribution

because of the high frictional resistance among particles with similar sizes. This agglomeration can cause blockages in CFB systems, resulting in unpredictable operations and decreased overall system capacity. Conversely, in the polydisperse case, particles smaller than the mean size are more easily returned to the riser by the return air, while larger particles remain in the loop seal. There was also a high-concentration area at the bottom of the riser in the monodisperse case, which is a typical mesoscale structure observed in gas-solid two-phase flows (Xiang & McGlinchey, 2004; Lan et al., 2013). Inertial collisions among particles of similar size consume more kinetic energy than collisions among particles of different sizes, contributing to the formation of mesoscale structures in the monodisperse case (Yang & Wang, 2020).

Figure 9 presents the axial distributions of the particle volume fraction for both cases in the riser. In general, the particle volume fraction exhibited a C-shaped distribution in the axial direction (Tu & Wang, 2017). The particle volume fraction is higher in the monodisperse case than that in the polydisperse case, except for regions below 0.2 m where larger and heavier particles are not easily entrained. The difference in the particle volume fraction between the two cases decreases gradually as the riser height increases; therefore, the effect of the particle size distribution can be negligible if the height is sufficiently large. Both cases predicted results similar to those of previous numerical studies (Zhang & Lu, 2019). The axial

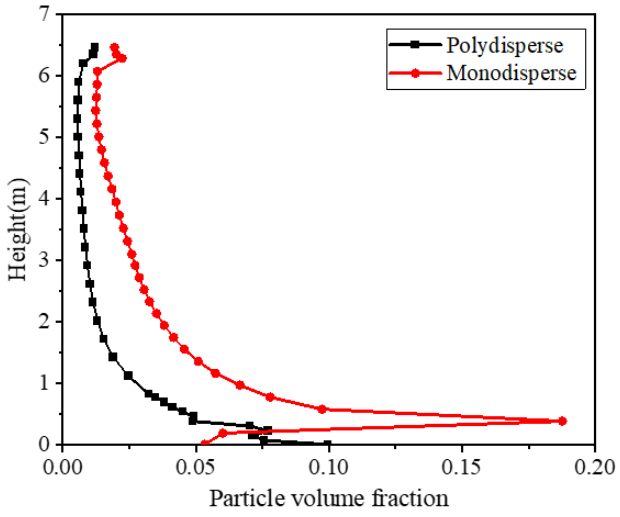

Fig. 9 Axial distributions of particle volume fraction in the riser

volume fraction distribution exhibited a significant fluctuation at approximately 0.5 m in the riser, indicating the strong influence of the unilateral return structure. In other words, the axial particle volume fraction distribution uniformity in the riser improved in the polydisperse system.

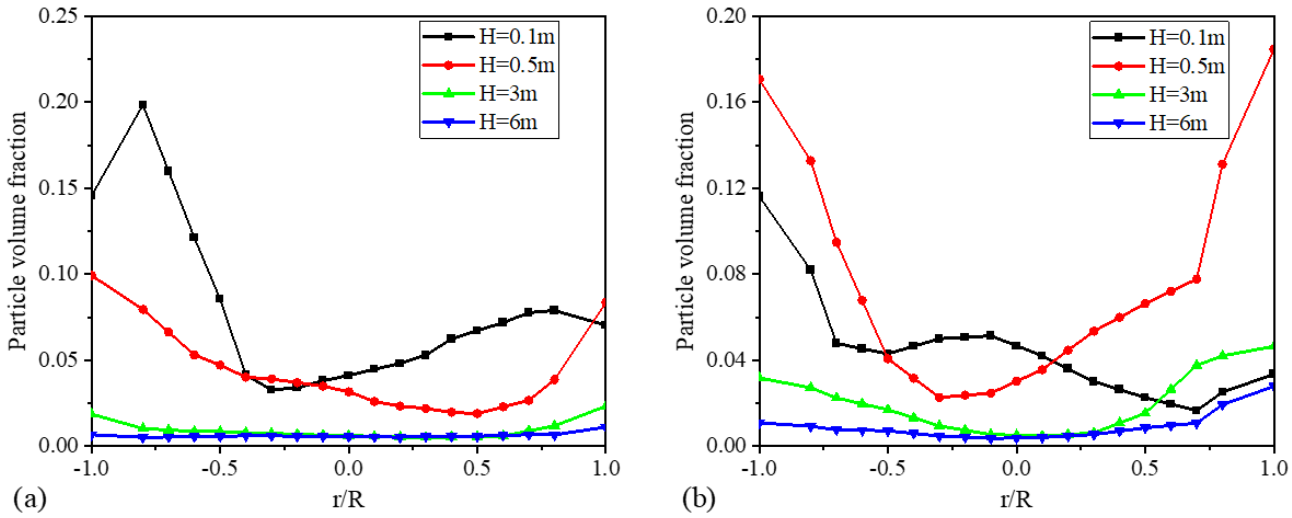

Fig. 10 Radial distributions of particle volume fraction at different riser heights: (a) polydisperse; (b) monodisperse

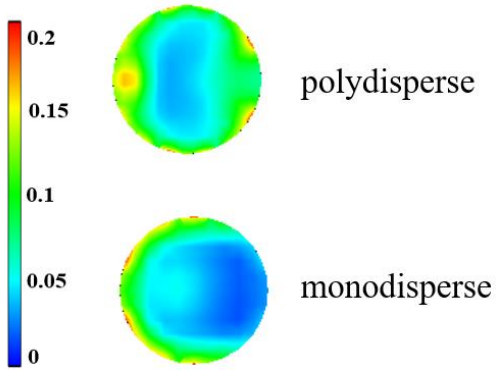

Fig. 11 Particle volume fraction distributions at H = 0.1 m for two particle size cases

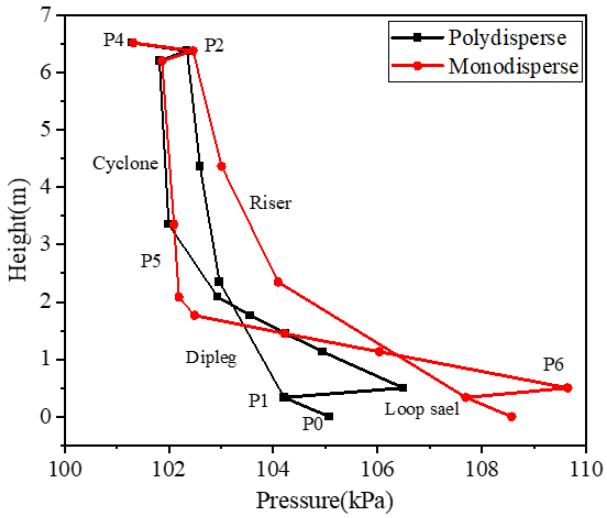

Fig. 12 Effect of particle size on distributions of full-loop time average pressure

The radial profiles of the particle volume fraction at different heights in the riser are displayed in Fig. 10. In general, the particles exhibit a "core-annular" flow structure with a dilute center and dense wall (Liu et al., 2017; Zhu et al., 2020). Some of the larger particles that were not entrained by the fluidized air were deposited at H = 0.1 m; therefore, the particle volume fraction was high at the bottom of the riser and asymmetric on both sides of the riser. As the height exceeded 3 m, this asymmetry diminished, and the radial particle volume fraction distribution tended to be linear, especially in the polydisperse case. Therefore, the polydisperse particle size distribution contributed to improving the radial particle volume fraction distribution uniformity. Figure 11 shows particle volume fraction distributions at H = 0.1 m for two particle size cases. It is noted that particles aggregate significantly near the left wall of the riser, but the particle clustering effect diminishes in the central region away from the wall in the polydisperse case. Therefore, the particle volume fraction initially increases and at r/R = -0.2 it decreases.

4.3.2 Pressure Distribution

Figures 12 and 13 illustrate the instantaneous and time averaged pressure distributions, for both cases. Figure 12 reveals that the pressure gradient in the standpipe is higher in the monodisperse case (Table 3). This can be attributed to a greater voidage when the particles size is uniform as opposed to different particle sizes. As shown in Fig. 13, the monodisperse case exhibits a deeper pressure coloring at the lower part of the CFB. Owing to large particle segregation at the bottom and the limited gas-carrying capacity, the pressure at the bottom of the riser was higher in the monodisperse case than in the polydisperse case. Moreover, the bed pressure drop in the riser was higher in the monodisperse system.

The impact of different particle size distributions on the pressure fluctuation was examined by analyzing a 15-s dataset of transient pressure, as shown in Fig. 14. The axial profile of the riser was divided into two distinct zones- a lower dense zone and an upper dilute zone–based on the particle volume fraction distribution. Two positions, 0.37 m (P1) and 6.40 m (P2) from the riser base were selected to study the pressure variations. In the polydisperse case, we observed small and moderate pressure fluctuations at P1 and P2, respectively. Moreover, the differences in the mean and standard deviations of the

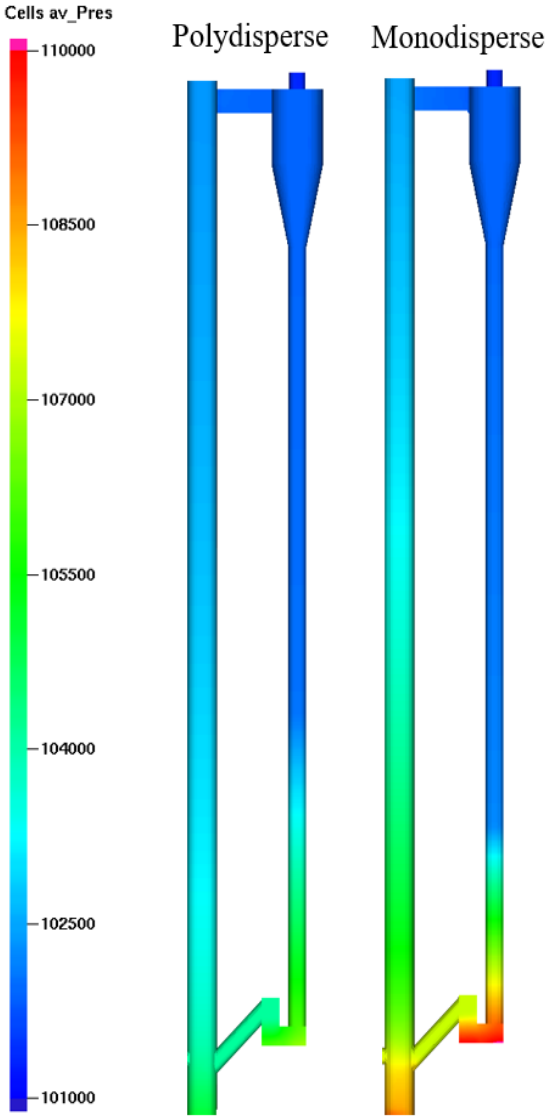

Fig. 13 Effect of particle size on instantaneous pressure distributions

pressure indicated variations in the flow characteristics. Specifically, compared to the monodisperse case, the mean pressure decreases by 3% at H = 0.37 m and by 0.2% at H = 6.4 m, and the mean pressure drop in the riser experiences a significant reduction of 63% in the polydisperse case. In addition, the standard deviation of the pressure signal serves as an indicator of fluidization quality in the CFB, and a lower standard deviation suggests superior bed fluidization (Sung et al., 2021). Therefore, the polydisperse case demonstrates a better fluidization quality than the monodisperse case, which supports previous findings (Shi et al., 2014; Li et al., 2022).

4.3.3 Particle Velocity Distribution

Figure 15 illustrates shows the radial time-averaged particle axial velocity distributions at various riser heights. Similar to previous findings (Shi et al., 2014; Yang et al., 2019c), the particles rose at high speeds in the central region and fell at low speeds near the walls. The particle axial velocity in the central region was lower in the polydisperse case than in the monodisperse case. This suggests that the particles have a long residence time in the central region, and that the contact efficiency between the gas and solid phases improved. The particles near the walls exhibited a significant downward axial velocity (H = 0.5 m) in the polydisperse case, which could cause strong back-mixing in this area. In the upper portion of the riser, the difference in particle axial velocity in the radial direction is slightly smaller in the polydisperse case, which implies a symmetric and uniform flow behavior.

4.4 Effect of Fuel Particle Mixing with Polydisperse Distributions

As discussed in Section 4.3, we observed a reduction in the pressure drop and a more uniform velocity distribution in the polydisperse system. Consequently, we investigated the effect of additional fuels, such as a mixture of coal and biomass, on the hydrodynamic characteristics of the CFB. The particle size distributions of various fuel particles are shown in Fig. 2, and five coal-biomass mass mixing ratios under different working conditions are listed in Table 4; it is worth noting that the total fuel mass remains the same.

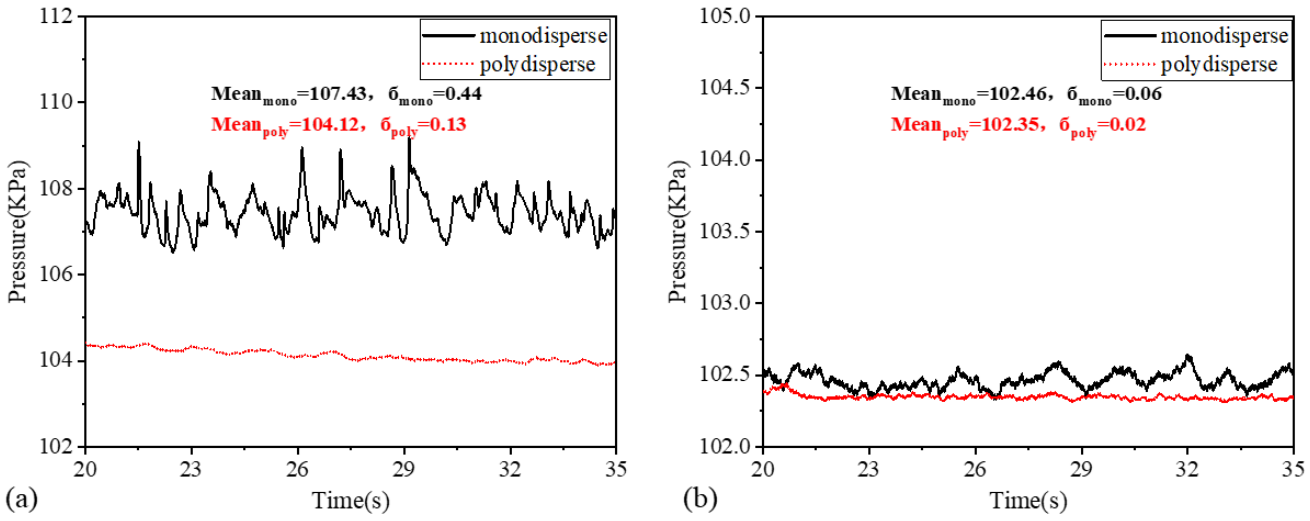

Fig. 14 Transient pressure predictions: (a) H=0.37m; (b) H =6.4m

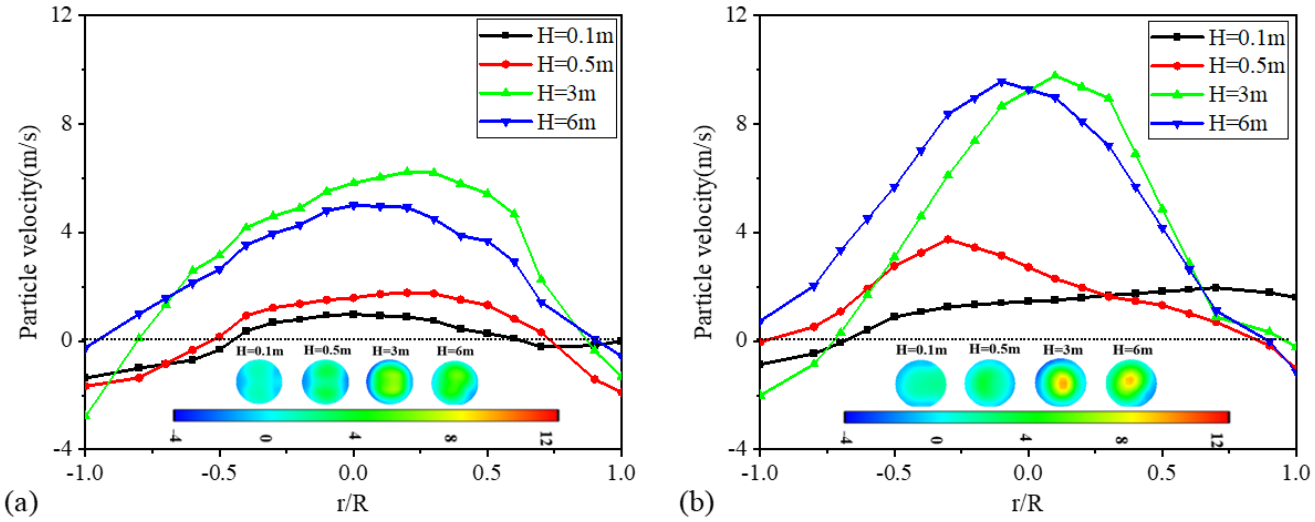

Fig. 15 Radial distributions of particle axial velocity at different riser heights: (a) polydisperse; (b) monodisperse

Table 4 Model condition used for the simulation cases

Simulation cases	Ratio of coal to biomass
Case 1	0:0
Case 2	10:0
Case 3	8:2
Case 4	5:5
Case 5	0:10

4.4.1 Particle Volume Fraction Distribution

The axial distribution of time-averaged particle volume fraction in the riser is shown in Fig. 16. The particle volume fraction changed significantly at the bottom of the riser, particularly after fuel particle addition. However, the particle volume fraction was relatively uniform and diluted above 2 m in the riser, regardless of whether fuel particles were added. This is mainly due to the fact that the particle back-mixing intensity is greatly reduced and the gas-solid momentum exchange is weakened in this region (Agrawal et al., 2001).

Snapshots of the transient particle volume fraction distribution at different riser cross-sections under the five operating conditions are present in Fig. 17. The riser exhibits a dense phase distribution at the bottom and a dilute phase distribution at the top in all cases (Ma et al., 2017). Upon fuel addition, the coal and biomass wide particle size distribution leads to an increased deposition of larger particles at the riser base. As a result, the concentration at H = 0.1 m is higher in Cases 2–5 than that in Case 1. A core-annular structure developed radially; the central region has a high particle concentration, while the wall region has a low particle concentration (Dymala et al., 2021). In all cases, some entrained upward-flowing particles moved from the center of the riser towards the wall, forming a dense region dominated by falling particles. After fuel addition, this dense region shrank, implying that the agglomeration effect weakened near the wall.

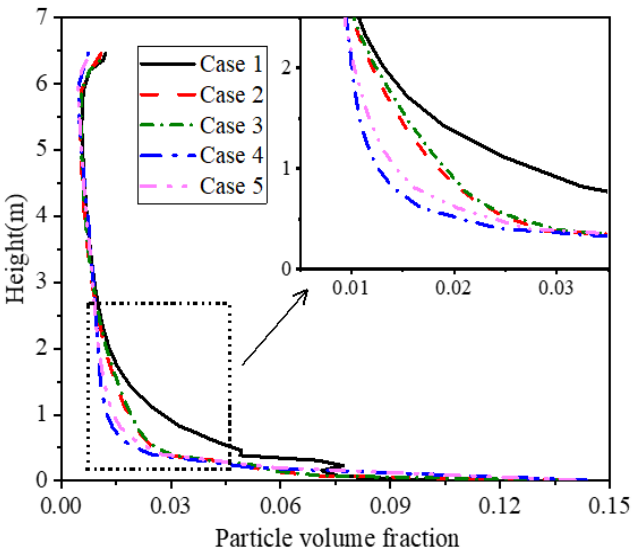

Fig. 16 Axial distributions of particle volume fraction in the riser

The radial time-average particle volume fractions at different riser heights are presented in Fig. 18. Figures 18 (a) and (b) show that the particle volume fraction between the two sides of the wall at heights of H = 0.1 and 0.5 m is clearly asymmetric in Case 1 due to the unilateral return flow structure. However, the radial particle volume fraction distribution curve leveled out in the other cases, indicating that the coal-distributed air counteracted the airflow entering from the unilateral return pipe. As displayed in Fig. 18 (c) and (d), the different particles are well mixed in the upper part of the riser regardless of the ratio of coal to biomass; therefore, the radial particle volume fraction distributions at different heights did not vary significantly.

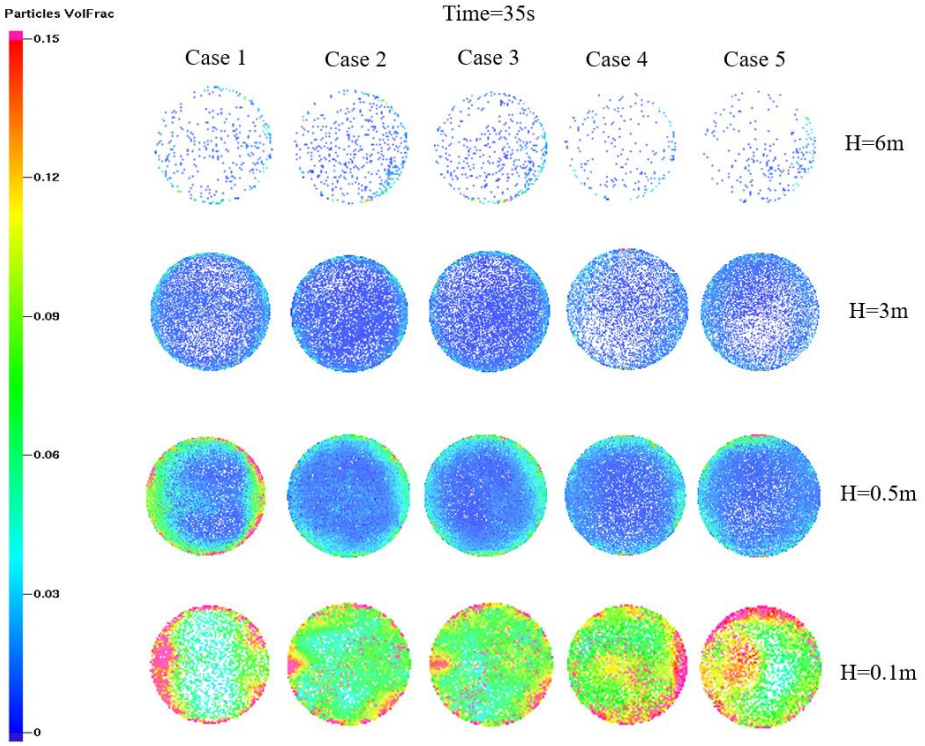

Fig. 17 Instantaneous distributions of particle volume fraction

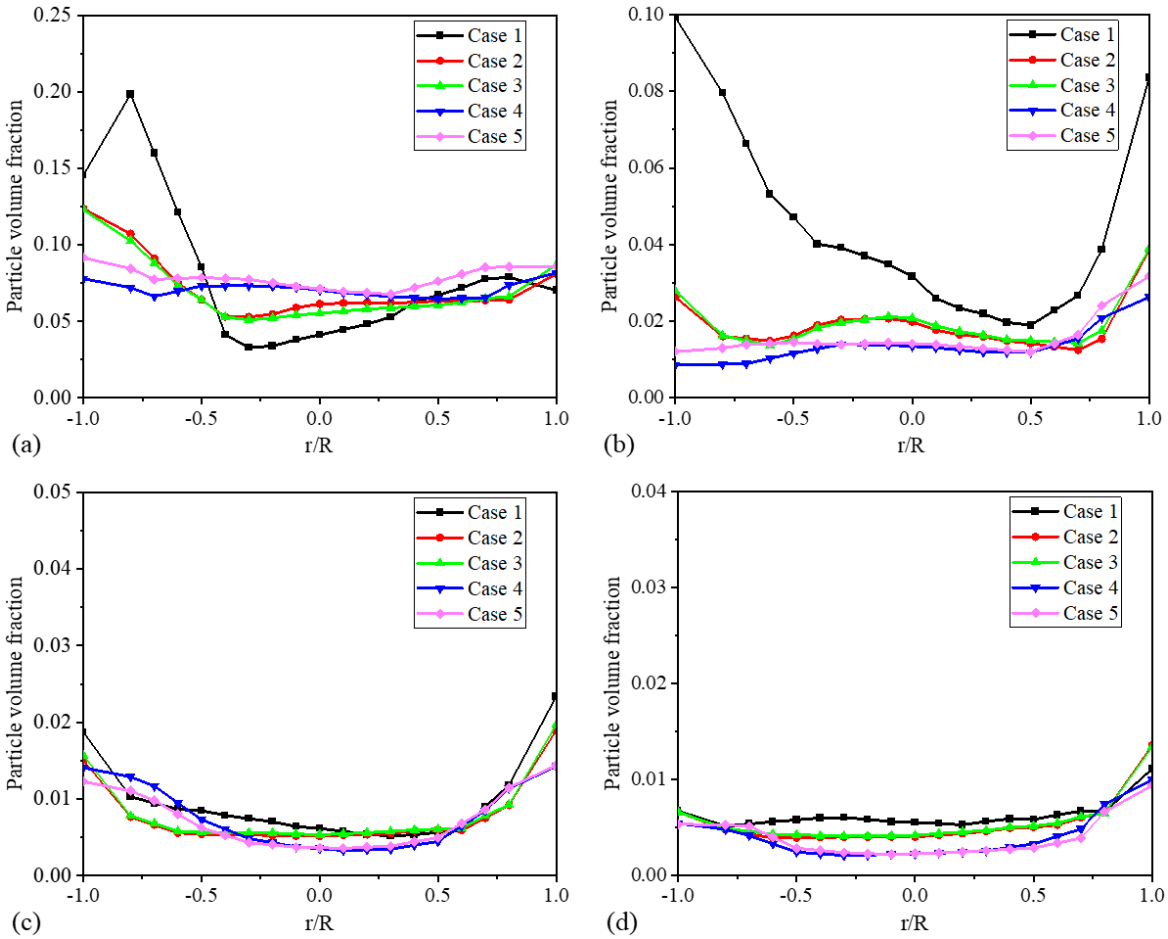

Fig. 18 Radial distributions of particle volume fraction at different riser heights: (a) H=0.1m; (b) H=0.5m; (c) H=3m; (d) H=6m

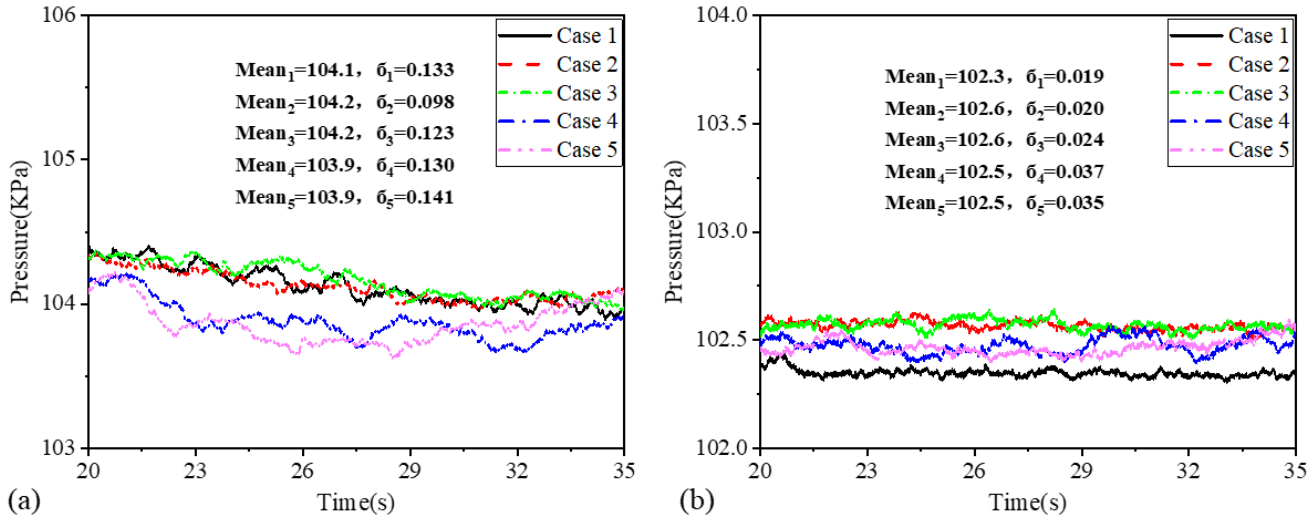

Fig. 19 Transient pressure predictions at different riser heights: (a) H=0.37m; (b) H=6.4m

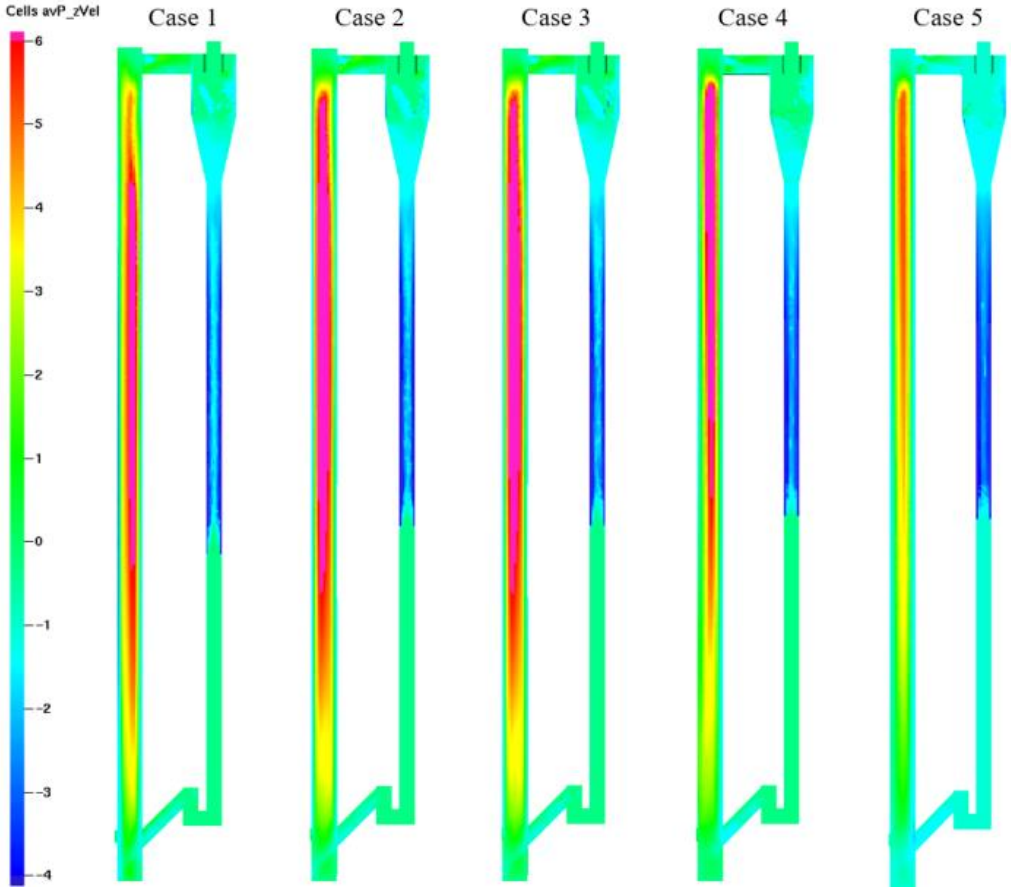

Fig. 20 Instantaneous distributions of particle axial velocity

4.4.2 Pressure Distribution

Figure 19 shows the transient pressure evolution at two specific locations, H = 0.37 m and H = 6.4 m, for the five cases. The pressure drop in the riser remained nearly constant at both locations when the biomass percentage changed from 0% to 20% or from 50% to 100%. However, a slight decrease in the pressure drop was observed as the biomass percentage increased from 20% to 50%.

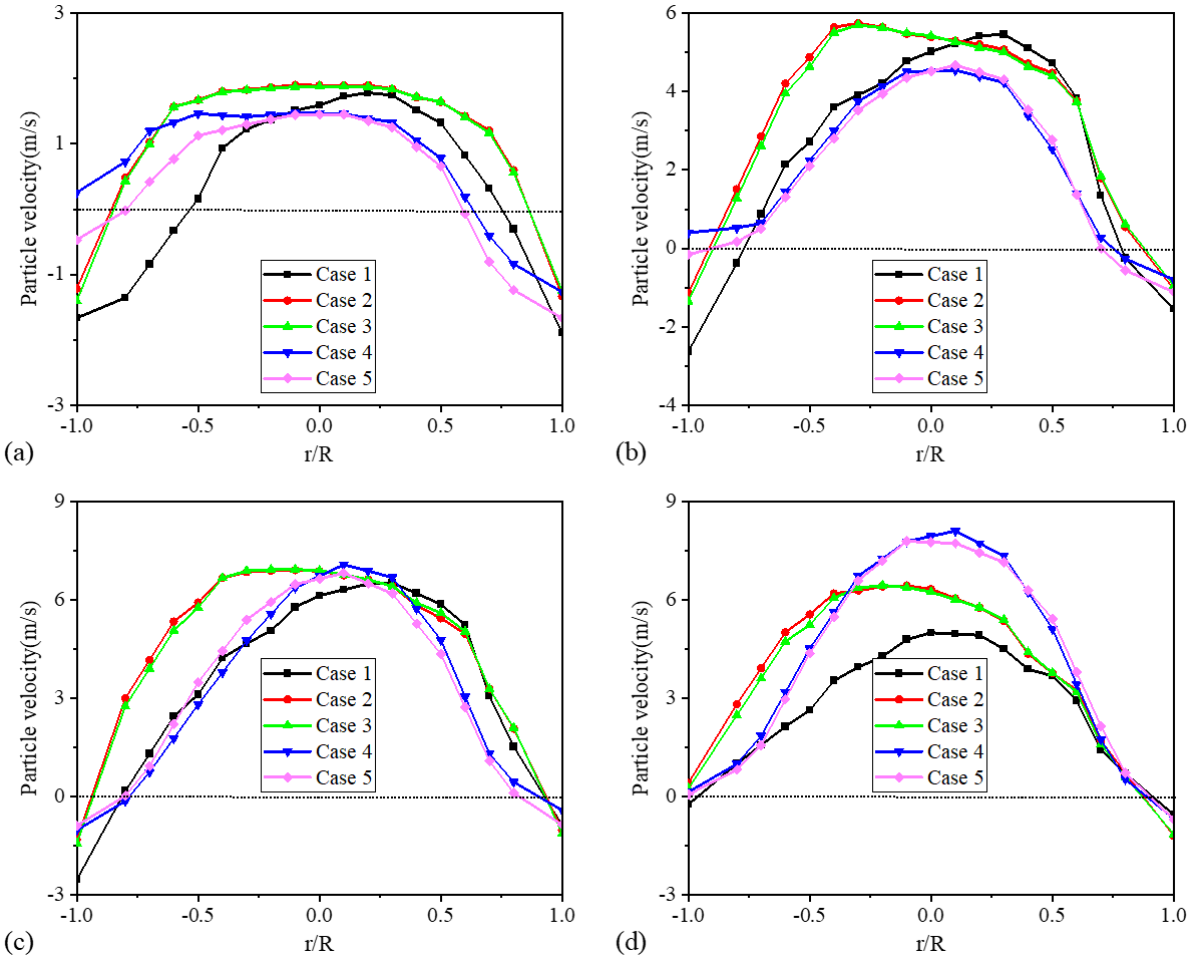

Fig. 21 Radial distributions of particle axial velocity at different riser heights: (a) H=0.1m; (b) H=0.5m; (c) H=3m; (d) H=6m

Furthermore, there is a noticeable reduction in the standard deviation of the pressure signal at H = 0.37 m when the biomass percentage is less than 50%, compared to the case without fuel addition, indicating an improvement in fluidization quality. Conversely, the standard deviation of the pressure signal at H = 6.4 m increases for a higher biomass proportion after fuel addition. This can be attributed to the intensified interactions between the small lightweight biomass particles in the upper part of the riser. Based on these findings, it is recommended that an excessive biomass mixing ratio be avoided when coupling coal and biomass fuels in CFBs.

4.4.3 Particle Velocity Distribution

Figure 20 illustrates the instantaneous particle axial velocity distributions. The particle axial velocity in the center region increased with fuel addition owing to the enhanced momentum exchange among particles. The velocity variation was minimal when the biomass proportion was less than 20%. However, as the biomass proportion increased, the high-velocity region shrank inward, and the length of the downward trailing region expanded, thereby extending the particle residence time. As the particles approach the riser outlet, they may collide with the top of the riser at high speeds, leading to momentum loss, change in the particle motion direction, and vortex formation (Chen et al., 2006).

Figure 21 shows the radial particle axial velocity distributions for the different cases. The particle velocities near the wall at all heights were significantly lower in Cases 2–5 than that in Case 1, implying that the back-mixing intensity at the wall was weakened by fuel addition. This is largely because a low particle volume fraction results in weaker interparticle collisions. The velocity distributions in Cases 2 and 3 were nearly identical, demonstrating that changing the biomass percentage from 0% to 20% had a negligible impact on the velocity distribution. However, when the biomass percentage reached 50% (Case 4), the opening of the parabola representing the velocity distribution narrowed, so that the velocity difference between the central and wall regions increased, which also led to an intensified lateral particle movement. In Cases 4 and 5, there is a relatively significant change in particle velocity at H = 0.5 m, likely due to chaotic flow at the bottom region of the riser caused by collisions among particles from loop-seal recirculation, upward transported particles by high-velocity airflow, and back-mixed particles near the wall.

5. CONCLUSIONS

In this study, the CPFD method was employed to compare flow behavior differences between polydisperse

and monodisperse systems, and to evaluate the effects of adding coal and biomass fuels at different mixing ratios on the gas-solid flow characteristics of a pilot CFB. The particle volume fraction, pressure, and velocity distributions were analyzed in detail. Based on the numerical results, the main conclusions of this study can be summarized as follows:

1. The particle volume fraction in both the monodisperse and polydisperse cases shows a C-shaped axial distribution and a radial distribution with a "core-annulus" structure (Liu et al., 2017). However, in the monodisperse case, the particles tended to accumulate at the circulation inlet and there was a region of relatively high concentration at the bottom of the riser. The monodisperse case exhibited fluctuations in the particle volume fraction at the return pipe structure, indicating axial nonuniformity of the particle volume fraction.

2. In polydisperse particle size systems, the particles have low velocities and long residence times. The flow behavior of the particles at the bottom of the riser differed significantly for the two particle size distribution conditions, as reported by Shi et al. (2014). The radial particle velocity distribution in the upper part of the riser was symmetrical and uniform. In addition, the numerical results show that the pressure drop in the riser, average pressure gradient in the standpipe, and particle circulation flux all decrease in the polydisperse case. The standard deviation of the pressure signal is smaller in the polydisperse case; thus, the fluidization quality of the CFB system is enhanced.

3. The mixing of multiple particles resulted in more particles being deposited at the bottom of the riser; however, the agglomeration effect and back-mixing intensity of the particles near the wall were weakened. With the addition of fuel particles and coal-distributed air, the radial particle volume fraction distribution became symmetrical and the disturbance at the circulation inlet decreased.

4. As the biomass ratio increased from 0% to 20% or from 50% to 100%, the particle volume fraction, pressure, and particle velocity distributions changed only slightly. When the biomass ratio is less than 50%, the standard deviation of the pressure signal was relatively small, indicating that the fluidization quality is better. Therefore, in terms of flow characteristics, the biomass mixing ratio should not be exceedingly large in future studies on the coupled combustion of coal and biomass.

Acknowledgement

This work was supported by the National Natural Science Foundation of China (Grant No. 51876092).

Conflict of Interest

The authors declare that they have no known competing financial interests or personal relationships that could have appeared to influence the work reported in this paper.

Authors Contribution

Qunxue Xiong: Methodology, Validation, Visualization, Writing-original draft. **Lin Zheng:** Conceptualization, Validation, Writing - review & editing.

References

Agrawal, K., Loezos, P. N., Syamlal, M., & Sundaresan, S. (2001). The role of meso-scale structures in rapid gas−solid flows. *Journal of Fluid Mechanics*, *445*, 151-185. https://doi.org/10.1017/S0022112001005663.

Almuttahar, A., & Taghipour, F. (2008a). Computational fluid dynamics of high density circulating fluidized bed riser: Study of modeling parameters. *Powder Technology*, *185*, 11-23. https://doi.org/10.1016/j.powtec.2007.09.010.

Almuttahar, A., &Taghipour, F. (2008b). Computational fluid dynamics of a circulating fluidized bed under various fluidization conditions. *Chemical Engineering Science*, *63*(6),1696-1709. https://doi.org/10.1016/j.ces.2007.11.020.

Alobaid, F. (2015). An offset-method for Euler−Lagrange approach. *Chemical Engineering Science*, *138*, 173-193. http://dx.doi.org/10.1016/j.ces.2015.08.010.

Bandara, J. C., Moldestad, B. M. E., & Eikeland, M. S. (2022). Circulating fluidized bed reactor− Experimental optimization of loop seal aeration and parametric study using CPFD simulations. *Powder Technology*, *405*, 117495. https://doi.org/10.1016/j.powtec.2022.117495.

Bhusarapu, S., Al-Dahhan, M. H., & Duduković, M. P. (2006). Solids flow mapping in a gas–solid riser: Mean holdup and velocity fields. *Powder Technology*, *163*, 98-123. https://doi.org/10.1016/j.powtec.2006.01.013.

Carlos Varas, A. E., Peters, E. A. J. F., & Kuipers, J. A. M. (2017). Experimental study of full field riser hydrodynamics by PIV/DIA coupling. *Powder Technology*, *313*, 402-416. https://doi.org/10.1016/j.powtec.2017.01.055.

Chen, C., Werther, J., Heinrich, S., Qi, H., & Hartge, E. (2013). CPFD simulation of circulating fluidized bed risers. *Powder Technology*, *235*, 238-247. https://doi.org/10.1016/j.powtec.2012.10.014.

Chen, Y., Tian, Z., & Miao, Z. (2006). Analysis of the pressure fluctuations in binary solids circulating fluidized bed. *Energy Conversion and Management*, *47*(5), 611-623. https://doi.org/10.1016/j.enconman.2005.05.013.

Córcoles, J. I., Acosta-Iborra, A., Almendros-Ibáñez, J. A., & Sobrino, C. (2021). Numerical simulation of a 3-D gas-solid fluidized bed: Comparison of TFM and CPFD numerical approaches and experimental validation. *Advanced Powder Technology*, *32* (10), 3689-3705. https://doi.org/10.1016/j.apt.2021.08.029.

Dong, P., Tu, Q., Wang, H., & Zhu, Z. (2021). Effects of pressure on flow characteristics in a pressurized circulating fluidized bed. *Particuology*, *59*, 16-23. https://doi.org/10.1016/j.partic.2020.07.004.

Dymala, T., Wytrwat, T., & Heinrich, S. (2021). MP-PIC simulation of circulating fluidized beds using an

EMMS based drag model for Geldart B particles. *Particuology*, *59*, 76-90. https://doi.org/10.1016/j.partic.2021.07.002.

Fan, R., Marchisio, D.L., & Fox, R.O. (2004). Application of the direct quadrature method of moments to polydisperse gas–solid fluidized beds. *Powder Technology*, *139*(1), 7-20. https://doi.org/10.1016/j.powtec.2003.10.005.

Gündüz, R. D., Yılmaz, B., & Özdoğan, S. (2020). Cold flow simulation of a 30 kW_{th} CFB riser with CPFD. *Journal of Applied Fluid Mechanics 13*(2), 603-614. https://doi.org/10.29252/jafm.13.02.30534.

Harris, S. E., & Crighton, D. G. (1994). Solitons, solitary waves, and voidage disturbances in gas-fluidized beds. *Journal of Fluid Mechanics*, *266*, 243-276. https://doi.org/ 10.1017/S0022112094000996.

Lan, X., Shi, X., Zhang, Y., Wang, Y., Xu, C., & Gao, J. (2013). Solids back-mixing behavior and effect of the mesoscale structure in CFB risers. *Industrial & Engineering Chemistry Research*, *52*, 11888-11896. https://doi.org/10.1021/ie3034448.

Leboreiro, J., Joseph, G. G., Hrenya, C. M., Snider, D. M., Banerjee, S. S., &Galvin, J. E. (2008). The influence of binary drag laws on simulations of species segregation in gas-fluidized beds. *Powder Technology*, *184*(3), 275-290. https://doi.org/10.1016/j.powtec.2007.08.015.

Li, S., Zhao, P., Xu, J., Zhang, L., & Wang, J. (2022). CFD-DEM simulation of polydisperse gas-solid flow of Geldart A particles in bubbling micro-fluidized beds. *Chemical Engineering Science*, *253*, 1177551. https://doi.org/10.1016/j.ces.2022.117551.

Li, T., Dietiker, J. F., & Shadle, L. (2014). Comparison of full-loop and riser-only simulations for a pilot-scale circulating fluidized bed riser. *Chemical Engineering Science*, *120*, 10-21. https://doi.org/10.1016/j.ces.2014.08.041.

Liu, C., Zhao, M., Wang, W., & Li, J. (2015). 3D CFD simulation of a circulating fluidized bed with on-line adjustment of mechanical valve. *Chemical Engineering Science*, *137*, 646-55. https://doi.org/10.1016/j.ces.2015.07.006.

Liu, D., & van Wachem, B. (2019). Comprehensive assessment of the accuracy of CFD-DEM simulations of bubbling fluidized beds. *Powder Technology*, *343*, 145-158. https://doi.org/10.1016/j.powtec.2018.11.025.

Liu, H. P., Bi, Y., Sun H. W., Zhang, L., Yang, F., & Wang Q. (2022). CPFD simulation of gas-solid flow in dense phase zone of pant-leg fluidized bed with secondary air. *Journal of Applied Fluid Mechanics*, *15*(5), 1319-1331. https://doi.org/10.29252/jafm.11.04.28397.

Liu, H., Li, J., & Wang Q. (2017). Simulation of gas–solid flow characteristics in a circulating fluidized bed based on a computational particle fluid dynamics model. *Powder Technology*, *321*, (132-142). http://dx.doi.org/10.1016/j.powtec.2017.07.040

Luo, K., Wu, F., Yang, S., Fang, M., & Fan, J. (2015). High-fidelity simulation of the 3-D full-loop gas–solid flow characteristics in the circulating fluidized bed. *Chemical Engineering Science*, *123*, 22-38. https://doi.org/10.1016/j.ces.2014.10.039.

Ma, Q., Lei, F., Xu, X., & Xiao, Y. (2017). Three-dimensional full-loop simulation of a high-density CFB with standpipe aeration experiments. *Powder Technology*, *320*, 574-585. https://doi.org/10.1016/j.powtec.2017.07.094.

Mathiesen, V., Solberg, T., & Hjertager, B. H. (2000). Predictions of gas/particle flow with an Eulerian model including a realistic particle size distribution. *Powder Technology*, *112*, 34-35. https://doi.org/ 10.1016/S0032-5910(99)00303-4.

Nikolopoulos, A., Nikolopoulos, N., Charitos, A., Grammelis, P., Kakaras, E., Bidwe, A. R., & Varela, G. (2013). High-resolution 3-D full-loop simulation of a CFB carbonator cold model. *Chemical Engineering Science*, *90*, 137-150. https://doi.org/10.1016/j.ces.2012.12.007.

Shi, X., Lan, X., Liu, F., Zhang, Y., & Gao, J. (2014). Effect of particle size distribution on hydrodynamics and solids back-mixing in CFB risers using CPFD simulation. *Powder Technology*, *266*, 135-143. https://doi.org/10.1016/j.powtec.2014.06.025.

Snider, D. M. (2001). An incompressible three-dimensional multiphase particle-in-cell model for dense particle flows. *Journal of Computational Physics*, *170*, 523-549. https://doi.org/10.1006/jcph.2001.6747.

Sung, W. C., Kim, J. Y., Chung, S. W., & Lee, D.H. (2021). Effect of particle size distribution on hydrodynamics of pneumatic conveying system based on CPFD simulation. *Advanced Powder Technology*, *32*(7), 2336-2344. https://doi.org/10.1016/j.apt.2021.05.010.

Tu, Q., & Wang H. (2017). CPFD study of a full-loop three-dimensional pilot-scale circulating fluidized bed based on EMMS drag model. *Powder Technology*, *323*, 534-547. https://doi.org/10.1016/j.powtec.2017.09.045.

Wang, Q., Yang, H., Wang, P., Lu, J., Liu, Q., Zhang, H., Wei, L., & Zhang, M. (2014a). Application of CPFD method in the simulation of a circulating fluidized bed with a loop seal, part I—Determination of modeling parameters. *Powder Technology*, *253*, 814-821. https://doi.org/10.1016/j.powtec.2013.11.041.

Wang, Q., Yang, H., Wang, P., Lu, J., Liu, Q., Zhang, H., Wei, L., & Zhang, M. (2014b). Application of CPFD method in the simulation of a circulating fluidized bed with a loop seal Part II—Investigation of solids circulation. *Powder Technology*, *253*. 822-828. https://doi.org/10.1016/j.powtec.2013.11.040.

Wang, S., Luo, K., Hu, C., Sun, L., & Fan, J. (2018). Effect of superficial gas velocity on solid behaviors in a full-loop CFB. *Powder Technology*, *333*, 91-105. https://doi.org/10.1016/j.powtec.2018.04.011.

Xiang, J., & McGlinchey, D. (2004). Numerical simulation of particle motion in dense phase pneumatic conveying. *Granular Matter*, *6*, 167-172.

https://doi.org/ 10.1007/s10035-004-0161-2.

Yang, S., & Wang, S. (2020). Eulerian-Lagrangian simulation of the full-loop gas-solid hydrodynamics in a pilot-scale circulating fluidized bed. *Powder Technology*, *369*, 223-237. https://doi.org/10.1016/j.powtec.2020.05.043.

Yang, S., Wang, S., Luo, K., Fan, J., & Chew, J. W. (2019a). Numerical investigation of the cluster property and flux distribution in three-dimensional full-loop circulating fluidized bed with multiple parallel cyclones. *Powder Technology*, *342*, 253-266. https://doi.org/10.1016/j.powtec.2018.10.009.

Yang, S., Wang, S., Luo, K., Fan, J., & Chen, J. W. (2019b). Numerical investigation of the back-mixing and non-uniform characteristics in the three-dimensional full-loop circulating fluidized bed combustor with six parallel cyclones. *Applied Thermal Engineering*, *153*, 524-535. https://doi.org/10.1016/j.applthermaleng.2019.03.032.

Yang, Y., Wu, H., Lin, W., Li, H., & Zhu, Q. (2018). An exploratory study of three-dimensional MP-PIC-based simulation of bubbling fluidized beds with and without baffles. (2018). *Particulogy*, *39*, 68-77. https://doi.org/10.1016/j.partic.2017.10.003.

Yang, Z., Zhang, Y., & Zhang, H. (2019c). CPFD simulation on effects of louver baffles in a two-dimensional fluidized bed of Geldart A particles. *Advanced Powder Technology*, *30*(11), 2712-2725. https://doi.org/10.1016/j.apt.2019.08.018.

Zhang, H., & Lu, Y. (2019). A computational particle fluid-dynamics simulation of hydrodynamics in a three-dimensional full-loop circulating fluidized bed: Effects of particle-size distribution. *Particuology*, *4*, 134-145. https://doi.org/10.1016/j.partic.2019.02.004.

Zhang, H., Li, W., Ma, Q., Zhang, Y., & Lei., F. (2020). Numerical study on influence of exit geometry in gas–solid flow hydrodynamics of HDCFB riser by CPFD. *Advanced Powder Technology*, *31*, 4005-4017. https://doi.org/10.1016/j.apt.2020.08.006.

Zhu, X., Dong, P., Tu, Q., Zhu, Z., Yang, W., & Wang, H. (2019). Investigation of gas-solid flow characteristics in the cyclone dipleg of a pressurised circulating fluidised bed by ECT measurement and CPFD simulation. *Measurement science & technology*, *30*, 54002. https://doi.org/10.1088/1361-6501/aafd7e.

Zhu, X., Dong, P., Tu, Q., Zhu, Z., Yang, W., & Wang, H. (2020). Investigation of gas-solids flow characteristics in a pressurised circulating fluidised bed by experiment and simulation. *Powder Technology*, *366*, 420-433. https://doi.org/10.1016/j.powtec.2020.02.047.